Shear flow over a protuberance on a plane wall

C. POZRIKIDIS
Department of Applied Mechanics and Engineering Sciences, University of California at San Diego, La Jolla, Ca 92093-0411, USA

Abstract. Simple shear flow over a protuberance with an axisymmetric shape projecting from a plane wall with its axis normal to the wall is studied by means of a boundary-integral method that is suitable for computing three-dimensional Stokes flow in axisymmetric domains. The problem is formulated in terms of a system of three scalar Fredholm integral equations of the first kind for the distribution of traction over the surface of the protuberance and the wall, and is solved by means of a boundary-element method. Numerical computations are performed for a family of protuberances whose exposed surface is a section of a sphere or of an oblate spheroid with its minor axis normal to the wall, and the results are in agreement with those of previous analytical computations for hemispherical and spherical shapes. The numerical computations provide accurate information on the hydrodynamic force and torque exerted on the protuberances due to the shear flow, and the distribution of shear stresses, and illustrate the kinematical structure of the flow with reference to the development of stagnation points and flow reversal.

1. Introduction

An accurate description of shear flow over a protuberance projecting from a plane surface is necessary for understanding, analyzing, and modeling several natural, engineering, and physiological situations and pertinent laboratory observations. Examples include flow over a particle or an impurity that has been captured on the surface of a collector, and flow over a protrusion modeling a solitary irregularity on a rough surface. Pertinent physiological applications include the growth of thrombosis in flow *in vivo* or in laboratory facilities, the removal of endothelium cells from their matrix after they have been exposed to mechanical stresses of sufficient duration and strength, and the deformation and dislodging of white and red blood cells adhering to the endothelium *in vivo* or to the walls of a flow channel *in vitro*.

In all of these applications, in order to develop appropriate mathematical models, obtain quantitative results, and interpret laboratory observations, it is necessary to have good estimates for the force and torque exerted on the protuberances, as well as for the distribution of shear stresses over the projecting surfaces and adjacent sections of the wall. This information is prerequisite, for example, for deriving macroscopic boundary conditions for flow over a rough surface, modeled as a plane wall with randomly distributed irregularities, for estimating the deformation of a cell that adheres to a wall, for deducing the magnitude of adhesion forces that anchor a particle to a solid surface, and for computing the rate of scalar transport due to convection.

Theoretical and computational studies of *two-dimensional* flow over protuberances with *cylindrical* shapes have been conducted on a number of occasions [1]. Such studies offer useful insights into the kinematical structure of the flow and illustrate the critical conditions for the onset of regions of recirculating flow, while maintaining the analytical effort and computational cost at an affordable level. Since, however, most applications of practical concern involve protuberances with compact shapes of finite extent, studies of three-dimensional flow are

desirable if not imperative. The need for such studies is underlined by the observation that the topology of three-dimensional reversed and separated flow has certain features that are absent from the corresponding two-dimensional motions. Examples include the occurrence of saddles and the formation of open streamlines that spiral into singular points [2].

Shear flow over a protuberance whose shape is a whole sphere that touches a plane wall, or over a hemisphere that is attached to a plane wall, have been analyzed on at least three previous occasions. O'Neill [3] developed an infinite-series solution for shear flow over a whole sphere, and computed the force and torque exerted on the sphere with high precision. Hyman [4] considered the corresponding flow over a hemispherical bump, but his solution was incomplete; later, in a corrigendum, the same author offered a qualitative correction to his original contribution. More recently, Price [5] improved Hyman's computations, derived the correct expression for the velocity field in the form of an infinite series, and obtained the correct value for the force and torque exerted on the protuberance. His interpretation of the structure of the flow in the vicinity of the base of the hemisphere, however, is partially but subtly incorrect, as will be shown by the results of the present numerical study. The distribution of shear stress over the surface of the protuberances and adjacent wall have not been discussed by previous authors.

The objective of the present paper is to provide accurate and extensive information on the structure of Stokes flow past protuberances with axisymmetric shapes; the restriction of axisymmetry is dictated by the particular implementation of the numerical method to be discussed in the next section, and could be waived at the expense of numerical efficiency and accuracy. To this end, it should be noted that accurate and extensive theoretical or computational studies of three-dimensional flow past protuberances have been hindered by analytical complexities and high computational cost. The former is due to difficulties in introducing families of boundary-fitted orthogonal curvilinear coordinates in which the governing equations admit separable solutions. The high computational cost is due to the virtually infinite or semi-infinite domain of flow, which requires the numerical discretization of a large volume of fluid or boundary-surface area in order to achieve an acceptable level of accuracy.

A recently developed boundary-integral formulation pertinent to three-dimensional Stokes flow in an axisymmetric domain, provides us with an efficient method for studying shear flow past protuberances with axisymmetric shapes. The method was discussed by the present author in reference [6] and was subsequently generalized and applied to problems of particle motions in a cell with parallel-sided walls, and flow over a wall with an axisymmetric cavity or an orifice of finite thickness [7,8]. Analogous methods are discussed by Kim and Karilla [9, Chapter 18]. One important step in the mathematical formulation is the representation of the flow in terms of a single-layer hydrodynamic potential of Stokes flow, expressing distributions of point-force singularities over natural or artificial boundaries of the flow. The process of constructing the single-layer representation depends upon the particular geometry of the domain of flow, and must be carried out on a case-by-case basis. Having developed the single-layer representation, we decompose the velocity field and boundary traction in complex Fourier series, and thus obtain systems of one-dimensional integral equations of the first kind for the unknown Fourier coefficients over the trace of the boundaries in an azimuthal plane.

The details of the mathematical formulation and the implementation of a simple yet effective numerical method of solution will be discussed in Section 2. In Section 3, we shall present and discuss results of numerical computations for protuberances whose surface is a section of sphere or oblate spheroid. The results for protuberances with hemispherical
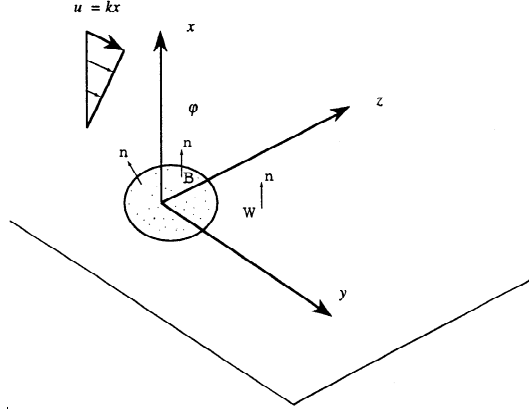
Figure 1. Schematic illustration of simple shear flow over a plane wall with an axisymmetric protuberance representing, for example, a particle adhering to the wall.

and spherical shapes will be compared with those of analytical computations conducted by previous authors, with excellent agreement.

2. Problem formulation and numerical method

Consider simple shear flow along the y axis varying along the x axis with velocity $\mathbf{u}^\infty = (0, kx, 0)$ past a protuberance of revolution that adheres to a plane wall with its axis normal to the wall in the x direction as illustrated in Figure 1, where k is the shear rate. The Reynolds number $Re = ka^2/\nu$, where a is the typical size of the protuberance and ν is the kinematic viscosity of the fluid, is assumed to be sufficiently small, so that the motion of the fluid is governed by the Stokes equation and the continuity equation

$$-\nabla P + \mu \nabla^2 \mathbf{u} = 0, \quad \nabla \cdot \mathbf{u} = 0, \tag{1}$$

where P is the modified pressure that incorporates the hydrostatic variations due to gravity, μ is the viscosity of the fluid, and $\mathbf{u}$ is the velocity [6]. The boundary conditions require that $\mathbf{u}$ vanish over all boundaries, including the surface of the protuberance denoted by P, and the infinite part of the wall that is not occupied by the protuberance in the yz plane denoted by W. Furthermore, the velocity must tend to that of the unperturbed shear flow $\mathbf{u}^\infty$ away from the projection.

We begin developing the solution by expressing the flow as the sum of the incident shear flow with the velocity $\mathbf{u}^\infty$ and a disturbance flow due to the protuberance with the velocity $\mathbf{u}^D$, writing $\mathbf{u} = \mathbf{u}^\infty + \mathbf{u}^D$. The disturbance velocity is required to vanish at infinity, and satisfy the boundary conditions $\mathbf{u}^D = \mathbf{0}$ over W, and $\mathbf{u}^D = -\mathbf{u}^\infty$ over D.

Next, we introduce a control volume that is enclosed by P, W, and a large surface that encloses the upper half-space, select a point $\mathbf{x}_0$ that lies within the control volume, and use the standard boundary-integral representation to express the velocity in terms of two distributions of singular solutions to the governing equations of Stokes flow, the single-layer and double-layer hydrodynamic potentials of Stokes flow [6]. In the limit, as the size of the large surface tends to infinity, we obtain

$$\mathbf{u}(\mathbf{x}_0) = \mathbf{u}^\infty(\mathbf{x}_0) - \frac{1}{8\pi\mu} \mathbf{I}^s(\mathbf{x}_0; \mathbf{f}^D, W) + \frac{1}{8\pi} \mathbf{I}^d(\mathbf{x}_0; \mathbf{u}^D, P), \tag{2}$$

where the superscripts s, d, D designate, respectively, the single-layer potential defined in Equation (3), the double-layer potential defined in Equation (4), and the disturbance flow. $\mathbf{f}^D$ is the disturbance boundary traction defined as $\mathbf{f}^D = \boldsymbol{\sigma}^D \cdot \mathbf{n}$, where $\boldsymbol{\sigma}^D$ is the stress tensor of the disturbance flow, and $\mathbf{n}$ is the unit normal vector pointing into the fluid as shown in Figure 1.

The hydrodynamic potentials shown in Equation (2) have the explicit forms

$$I_i^s(\mathbf{x}_0; \mathbf{f}, S) = \int_S G_{ij}(\mathbf{x}_0, \mathbf{x}) f_j(\mathbf{x}) \, \mathrm{d}S(\mathbf{x}) \tag{3}$$

and

$$I_i^d(\mathbf{x}_0; \mathbf{u}, S) = \int_S u_j(\mathbf{x}) T_{jik}(\mathbf{x}, \mathbf{x}_0) n_k(\mathbf{x}) \, \mathrm{d}S(\mathbf{x}), \tag{4}$$

where $\mathbf{G}$ and $\mathbf{T}$ are the free-space Green's function of the equations of Stokes flow for the velocity and stress, given respectively by

$$G_{ij}(\mathbf{x}_0, \mathbf{x}) = \frac{\delta_{ij}}{|\hat{\mathbf{x}}|} + \frac{\hat{x}_i \hat{x}_j}{|\hat{\mathbf{x}}|^3} \qquad T_{jik}(\mathbf{x}_0, \mathbf{x}) = -6 \frac{\hat{x}_j \hat{x}_i \hat{x}_k}{|\hat{\mathbf{x}}|^5} \tag{5}$$

and where $\hat{\mathbf{x}} = \mathbf{x} - \mathbf{x}_0$ ([6]). Physically, Equations (3) and (4) represent distributions of singular solutions of the equations of Stokes flow including the point force and the stresslet. The latter is derived from the point-force dipole.

Next, we select as a control volume the volume occupied by the protuberance, apply the reciprocal theorem of Stokes flow for the incident shear flow and the flow due to a point force placed at the same point $\mathbf{x}_0$, and note that $\mathbf{u}^\infty = \mathbf{0}$ over the part of the wall that is occupied by the protuberance, which is denoted by B standing for "*Base*". We thus obtain

$$-\frac{1}{8\pi\mu} \mathbf{I}^s(\mathbf{x}_0; \mathbf{f}^\infty, P) + \frac{1}{8\pi\mu} \mathbf{I}^s(\mathbf{x}_0; \mathbf{f}^\infty, B) + \frac{1}{8\pi} \mathbf{I}^d(\mathbf{x}_0; \mathbf{u}^\infty, P) = 0, \tag{6}$$

where $\mathbf{f}^\infty = \boldsymbol{\sigma}^\infty \cdot \mathbf{n}$, and the unit normal vector $\mathbf{n}$ over B points into the upper half-space [6]. We note that the velocity vanishes over P, and add the right-hand side of Equation (6) to the right-hand side of Equation (2) to obtain a representation for the velocity in terms of a collection of single-layer potentials, given by

$$\mathbf{u}(\mathbf{x}_0) = \mathbf{u}^\infty(\mathbf{x}_0) + \frac{1}{8\pi\mu} \mathbf{I}^s(\mathbf{x}_0; \mathbf{f}^\infty, B) - \frac{1}{8\mu\pi} \mathbf{I}^s(\mathbf{x}_0; \mathbf{f}, P) - \frac{1}{8\pi\mu} \mathbf{I}^s(\mathbf{x}_0; \mathbf{f}^D, W). \tag{7}$$

The individual potentials represent distributions of point forces, with distribution densities equal to the corresponding boundary tractions.

Having developed the single-layer representation, we expand the cylindrical polar components of the velocity and boundary traction in complex Fourier series with respect to the azimuthal angle φ over each axisymmetric sub-domain B, P, and W, writing

$$u_\alpha(x, \sigma, \varphi) = \sum_{n=-\infty}^{\infty} \hat{u}_{\alpha n}(x, \sigma) e^{in\varphi}, \qquad f_\alpha(l, \varphi) = \sum_{n=-\infty}^{\infty} \hat{f}_{\alpha n}(l) e^{in\varphi}, \tag{8}$$

where a Greek index stands for x, or σ, or φ. In the expansion for the boundary traction, l represents the arc length along the trace of a sub-domain in an azimuthal plane measured from an arbitrary point. Substituting the expansions given in Equations (8) in Equation (7),

and collecting Fourier coefficients of identical orders, yields an integral representation for the Fourier coefficients in the form

$$
\begin{aligned}
\hat{u}_{\alpha n}(x_0, \sigma_0) \;=\; & \hat{u}_{\alpha n}^{\infty}(x_0, \sigma_0) + \frac{1}{8\pi\mu} \int_{T_B} Q_{\alpha\beta n}(\hat{x}, \sigma, \sigma_0)\hat{f}_{\beta n}^{\infty}(l)\sigma \, \mathrm{d}l \\
& -\frac{1}{8\pi\mu} \int_{T_W} Q_{\alpha\beta n}(\hat{x}, \sigma, \sigma_0)\hat{f}_{\beta n}^{D}(l)\sigma \, \mathrm{d}l \\
& -\frac{1}{8\pi\mu} \int_{T_p} Q_{\alpha\beta n}(\hat{x}, \sigma, \sigma_0)\hat{f}_{\beta n}(l)\sigma \, \mathrm{d}l,
\end{aligned}
\tag{9}
$$

where $\hat{x} = x - x_0$; T_B, T_P, T_W are the traces of the under-subscribed surfaces in the xy plane corresponding to $\varphi = 0$, and repeated Greek, but not Roman, subscripts are summed over x, σ, and φ. The computation of the kernel matrix $Q_{\alpha\beta n}$ is discussed in Section 2.4 of ref. [6] and chapter 18 of ref. [9].

In the particular case of simple shear flow along the y axis under present consideration, the cylindrical polar components of the velocity exhibit harmonic dependencies on the azimuthal angle φ in the form

$$
u_x = kaG_x(x, \sigma)\cos\varphi, \qquad u_\sigma = kaG_\sigma(x, \sigma)\cos\varphi, \qquad u_\varphi = -kaG_\varphi(x, \sigma)\sin\varphi,
\tag{10}
$$

where G_x, G_σ, and G_φ are three real dimensionless functions. For example, the unperturbed incident shear flow, $\mathbf{u}^\infty = (0, kx, 0)$, corresponds to $G_x^\infty = 0$, $G_\sigma^\infty = x/a$, $G_\varphi^\infty = x/a$. The associated complex Fourier coefficients introduced in Equation (8) are given by

$$
\hat{u}_{x1} = \hat{u}_{x(-1)} = \frac{1}{2} kaG_x, \quad \hat{u}_{\sigma 1} = \hat{u}_{\sigma(-1)} = \frac{1}{2} kaG_\sigma, \quad \hat{u}_{\varphi 1} = -\hat{u}_{\varphi(-1)} = \frac{1}{2} kaiG_\varphi,
\tag{11}
$$

whereas all other Fourier coefficients are equal to zero.

The linearity of Equation (9) suggests that, correspondingly, all but the first-order Fourier coefficients of the boundary traction vanish and, furthermore, it dictates setting

$$
\hat{f}_{x1} = \hat{f}_{x(-1)} \equiv \frac{1}{2} \mu k H_x, \quad \hat{f}_{\sigma 1} = \hat{f}_{\sigma(-1)} \equiv \frac{1}{2} \mu k H_\sigma, \qquad \hat{f}_{\varphi 1} = -\hat{f}_{\varphi(-1)} \equiv \frac{1}{2} \mu k i H_\varphi,
\tag{12}
$$

where H_x, H_σ, and H_φ are three real dimensionless functions. These expressions yield sinusoidal dependencies of the cylindrical polar components of the boundary traction upon the azimuthal angle, in the form

$$
f_x(l, \varphi) = \mu k H_x(l)\cos\varphi, \quad f_\sigma(l, \varphi) = \mu k H_\sigma(l)\cos\varphi, \quad f_\varphi(l, \varphi) = -\mu k H_\varphi(l)\sin\varphi.
\tag{13}
$$

Substituting the expressions given in Equations (10) and (13) in Equation (9) and simplifying, we obtain the integral representations of the Fourier coefficients of the velocity in terms of the Fourier coefficients of the boundary surface traction, given by

$$
G_\alpha(x_0, \sigma_0) \;=\; G_\alpha^\infty(x_0, \sigma_0) + \frac{1}{8\pi a} \int_{T_B} \Phi_{\alpha\beta}(\hat{x}, \sigma, \sigma_0)H_\beta^\infty(l)\sigma \, \mathrm{d}l(x)
$$

$$-\frac{1}{8\pi a}\int_{T_W}\Phi_{\alpha\beta}(\hat{x},\sigma,\sigma_0)H_\beta^D(l)\sigma\;\mathrm{d}l(x)$$

$$-\frac{1}{8\pi a}\int_{T_p}\Phi_{\alpha\beta}(\hat{x},\sigma,\sigma_0)H_\beta(l)\sigma\;\mathrm{d}l(x). \tag{14}$$

The kernel $\boldsymbol{\Phi}$ of the integral representation is found by straightforward algebraic manipulations to be

$$\Phi_{\alpha\beta}=\begin{bmatrix} I_{11}+\hat{x}^2 I_{31} & \hat{x}(\sigma I_{31}-\sigma_0 I_{32}) & \hat{x}\sigma_0(I_{32}-I_{30}) \\ \hat{x}(\sigma I_{32}-\sigma_0 I_{31}) & I_{12}+(\sigma_0^2+\sigma^2)I_{32}-\sigma\sigma_0(I_{33}+I_{31}) & I_{10}-I_{12}+\sigma_0^2(I_{30}-I_{32}) \\ & & -\sigma\sigma_0(I_{31}-I_{33}) \\ \hat{x}\sigma(I_{30}-I_{32}) & I_{10}-I_{12}+\sigma^2(I_{30}-I_{32}) & I_{12}+\sigma\sigma_0(I_{31}-I_{33}) \\ & -\sigma\sigma_0(I_{31}-I_{33}) & \end{bmatrix}, \tag{15}$$

where $\hat{x}=x-x_0$,

$$I_{mn}(\hat{x},\sigma,\sigma_0)\equiv\int_0^{2\pi}\frac{\cos^n\omega}{[\hat{x}^2+\sigma^2+\sigma_0^2-2\sigma\sigma_0\cos\omega]^{m/2}}\;\mathrm{d}\omega$$

$$=\frac{4w^m}{(4\sigma\sigma_0)^{m/2}}\int_0^{\pi/2}\frac{(2\cos^2\omega-1)^n}{(1-w^2\cos^2\omega)^{m/2}}\;\mathrm{d}\omega \tag{16}$$

and

$$w^2=\frac{4\sigma\sigma_0}{\hat{x}^2+(\sigma+\sigma_0)^2}. \tag{17}$$

The integrals on the right-hand side of Equation (16) may be expressed in terms of complete elliptic integrals of the first and second kinds which, in turn, may be computed using either fast iterative methods or polynomial approximations [10, p 591].

The Fourier coefficients of the traction over the base B corresponding to the incident flow are given by $H_x^\infty=0$, $H_\sigma^\infty=1$, $H_\varphi^\infty=1$. These values may be used to compute the first integral on the left-hand side of Equation (14), which then becomes a known.

Taking the limit of Equation (14) as the point $\mathbf{x}_0$ approaches the wall or the surface of the protuberance, and requiring that the boundary velocity vanish, we obtain the following set of three one-dimensional real Fredholm integral equations of the first kind for the Fourier coefficients corresponding to the boundary distribution of the total or disturbance surface traction,

$$\int_{T_w}\Phi_{\alpha\beta}(\hat{x},\sigma,\sigma_0)H_\beta^D(l)\sigma\;\mathrm{d}l(x)+\int_{T_p}\Phi_{\alpha\beta}(\hat{x},\sigma,\sigma_0)H_\beta(l)\sigma\;\mathrm{d}l(x)$$

$$=8\pi a G_\alpha^\infty(x_0,\sigma_0)+\int_{T_B}\Phi_{\alpha\beta}(\hat{x},\sigma,\sigma_0)H_\beta^\infty(l)\sigma\;\mathrm{d}l(x), \tag{18}$$

where, as mentioned before, $G_x^\infty=0, G_\sigma^\infty=x/a, G_\varphi^\infty=x/a$. The right-hand side of Equation (18) represents a known forcing function; the unknowns H_β^D and H_β have been collected on the left-hand side.

Once the integral equation (18) has been solved, the results are substituted in Equation (14) to produce the velocity at any point in the flow. To compute the y component of the force exerted on the protuberance, we use the expansion (13) and find

$$F_y=\pi\mu k\int_{T_P}[H_\sigma(l)+H_\varphi(l)]\sigma\;\mathrm{d}l(x). \tag{19}$$

The corresponding x and z components vanish. Working in a similar manner, we find that the z component of the torque with respect to a certain point that lies on the x axis at $x = x_c$ is given by

$$T_z = \pi \mu k \int_{T_C} [(x - x_c)(H_\sigma(l) + H_\varphi(l)) - \sigma H_x(l)] \sigma \, \mathrm{d}l(x). \tag{20}$$

The corresponding x and y components vanish.

2.1. NUMERICAL METHOD

To solve the integral equation (18), we have implemented a standard boundary-element collocation method [6]. Briefly, we discretize the contours T_B, T_W, and T_P into a set of boundary elements that are either straight segments or circular arcs, assume that H_α is constant over each element, and apply Equation (18) at the mid-point of each element to obtain a system of linear algebraic equations for the values H_α over all elements. The regular boundary integrals are computed by the six-point Gauss-Legendre quadrature. The singularities of the singular integrals are subtracted off and integrated analytically before the numerical quadrature is applied. The numerical method was shown to be second-order accurate with respect to the number of boundary elements. The details are straightforward and are omitted in the interest of saving space.

   The size of the elements is chosen so as to obtain adequate accuracy near corners and thus resolve the fine structure of the flow. Typically, we use 32 elements over the trace of the protuberance, and 64 elements over the wall; the ratio between the largest and smallest element size over the protuberance or wall is set equal to two, five, or ten. The length of the intervening elements increases geometrically by an appropriate constant factor. Furthermore, the wall contour C_W is truncated at a finite distance from the origin, typically set equal to fifteen times the characteristic protuberance size A to be defined in the next section. We compute the streamlines by integrating the velocity field, using either the second-order or fourth-order Runge-Kutta method; the integrals in Equations (19) and (20) are computed by the trapezoidal rule, which is consistent with the piece-wise constant approximation of the unknowns in the integral equation.

   All computations were performed on a SUN-SPARC station IPC with 24MB of RAM. A typical computation involved approximately 100 boundary elements and required less than 1 minute of CPU time. A corresponding velocity evaluation required a fraction of a second. This high performance attest to the efficiency of the mathematical formulation and numerical method of solution.

3.   Results and discussion

First, we consider simple shear flow over a protuberance that has the shape of a section of sphere of radius a and semi-angle $\alpha \pi$, depicted in Figure 3(a); $\alpha = 1.0$ yields a whole sphere, and $\alpha = 1/2$ yields a hemisphere.

3.1. FORCE AND TORQUE

In Table 1 we present the y component of the force, F_y, the z component of the torque with respect to the origin, T_z, and the z component of the torque with respect to the center of the sphere, M_z, acting on the protuberance, all accurate up to the third significant figure. For the

Table 1. The y component of the force, F_y, the z component of the torque with respect to the origin, T_z, and the z component of the torque with respect to the center of a spherical protuberance, M_z, exerted on a spherical protuberance of radius a and semi-angle $\alpha\pi$

α	$F_y/\pi\mu ka^2$	$T_z/\pi\mu ka^3$	$M_z/\pi\mu ka^3$
1.0	10.2	14.0	3.78
0.9	9.92	13.2	3.76
0.8	9.07	11.0	3.65
0.7	7.73	7.96	3.42
0.6	6.06	4.88	3.01
0.5	4.30	2.44	2.44
0.4	2.69	0.933	1.76
0.3	1.41	0.240	1.07
0.2	0.555	0.031	0.481
0.1	0.118	0.008	0.113

spherical shape corresponding to $\alpha = 1$, the results are in perfect agreement with the more accurate predictions of O'Neill [3] who finds $F_y = 10.205\pi\mu ka^2$ and $M_z = 3.776\pi\mu ka^3$. For the hemispherical shape corresponding to $\alpha = 1/2$, the numerical results coincide with, and have the same accuracy as those of Price [5], obtained using an analytical method. The agreement in these two extreme cases raises the level of confidence in, and demonstrates the accuracy and reliability of the numerical method.

In estimating the hydrodynamic force exerted on a particle that adheres to a wall, one might approximate it with the force exerted on the base of the particle due to the unperturbed shear flow. The results of Table 1 suggest that this approximation may lead to significant error. For example, for flow over a hemispherical particle, this simplified approach leads to a drag force coefficient equal to unity, instead of the correct value of 4.30. This important discrepancy suggests that simplified estimates for the shear stress exerted on the surface of the particle will carry a comparable degree of error and may lead to erroneous interpretations; this occurrence will be confirmed in the subsequent discussion. The discrepancies decrease as the maximum height of the cell is diminished, but there is still a substantial error for protuberances with small but finite height.

It is useful to compare the results for the force and torque acting on the hemispherical protuberance with the force and torque per unit width acting on a cylindrical protuberance whose cross section is a semi-circle of radius a. Davis & O'Neill [11] found that the coefficients corresponding to the values 4.30 and 2.44 shown in Table 1 are respectively equal to 4.00 and 2.00, which is somewhat, but not drastically, different from the values for three-dimensional flow.

3.2. WALL SHEAR STRESS

In Figures 2(*a–d*), we plot with solid lines the distribution of the dimensionless shear stress along the trace of the protuberance and wall in the xy plane, $\Sigma_y = \sigma_z/k\mu$, and with dashed lines the corresponding distribution of shear stress along the boundary trace in the xz plane, $\Sigma_y = \sigma_y/k\mu$, both with respect to the reduced arc length $l/\pi a$ measured along the respective traces of the wall, with origin at the top of the protuberance. The two distributions are distinct,
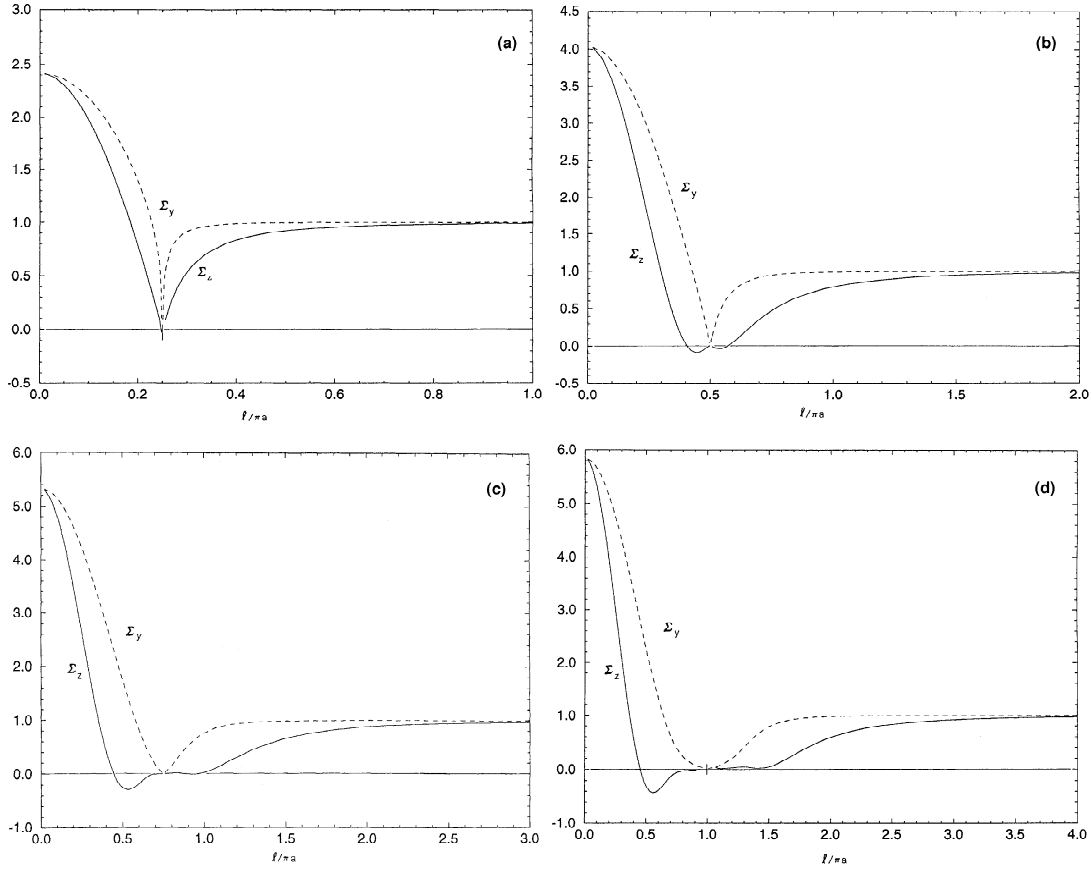
Figure 2. Shear flow over a protuberance whose shape is a section of a sphere of radius a and semi-angle $\alpha\pi$ as depicted in Figure 3. Solid lines show the dimensionless shear stress along the trace of the protuberance and of the wall in the xy plane, $\Sigma_z = \sigma_z/k\mu$, and dashed lines show the dimensionless shear stress along the corresponding boundary trace in the xz plane, $\Sigma_y = \sigma_y/k\mu$. Both are plotted with respect to reduced arc length, $l/\pi a$, measured along the respective traces of the boundary with origin at the top of the protuberance; (*a*) $\alpha = 0.25$, (*b*) 0.50, (*c*) 0.75, (*d*) 1.0.

but take a common value at the axis of symmetry where the tangential plane to the sphere is parallel to the wall. The corresponding protuberance shapes are shown in Figures 3(*a–d*).

Figure 2(*a*) reveals that the shear stress at the top of a relatively short protuberance with $\alpha = 0.25$ increases by a factor of nearly 2.5 with respect to the undisturbed value. The values of both Σ_z and Σ_y are positive over the main portion of the two traces of the protuberance, which indicates that the streamlines follow the topography of the boundary. Over the plane wall, the shear stress settles to the unperturbed values a relatively short distance away from the rim that is comparable to the size of the protuberance. Far from the protuberance, the velocity field due to the protuberance behaves like that due to a point-force dipole, and it thus decays like $1/r^2$, where r is the distance from the origin; the image system due to the wall takes up the point-force singularity associated with the drag force exerted on the protuberance [6]. The corresponding wall shear stress decays like $1/r^3$, which is consistent with the rapid algebraic decay observed in the results of the numerical computations.

Sufficiently close to the intersection between the protuberance and the wall, the flow in the xy plane is similar to two-dimensional antisymmetric flow between two intersecting planes forming a wedge whose aperture is equal to $(1 - \alpha)\pi$, for which an analytical solution
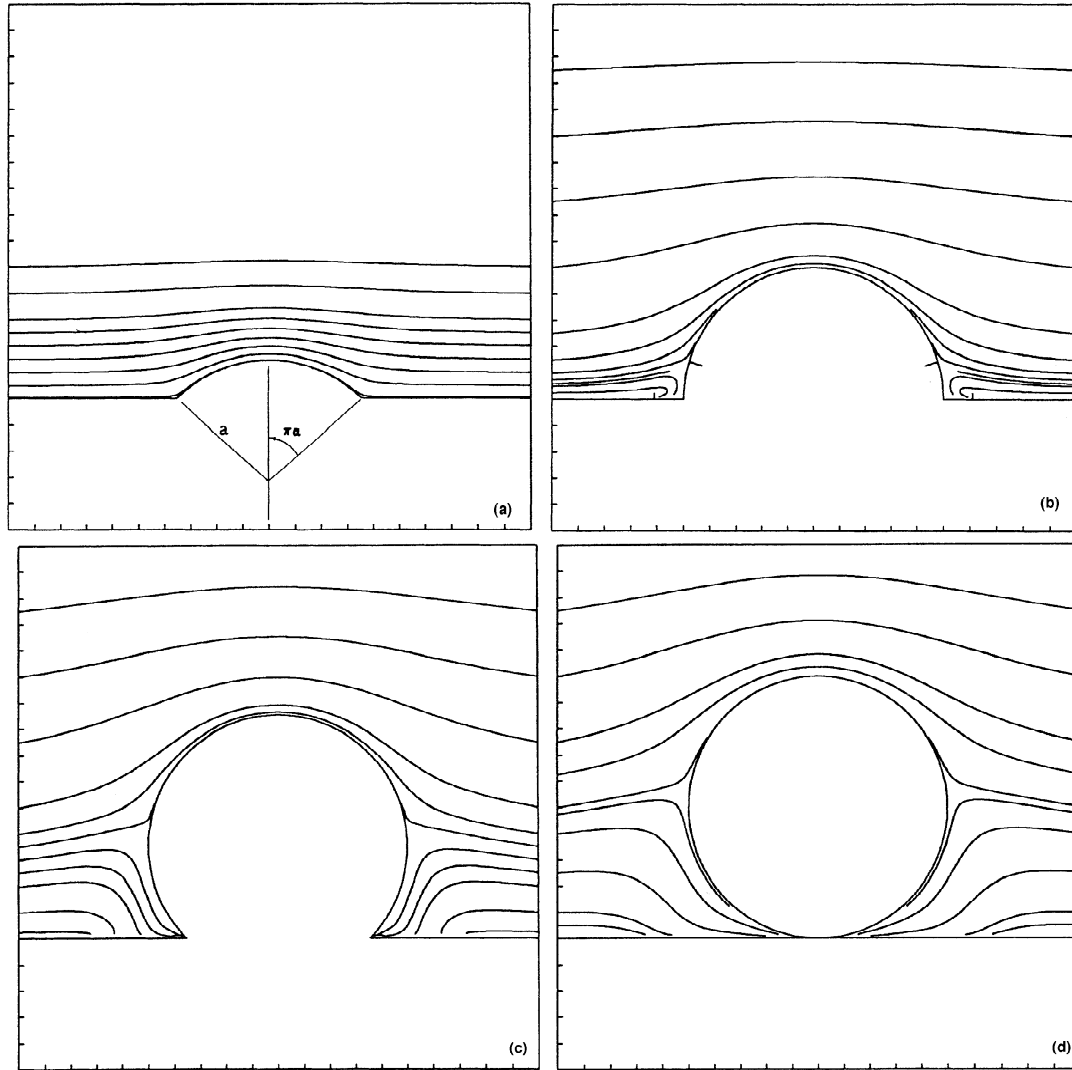
Figure 3. Streamline patterns in the xy mid-plane of flow over a spherical protuberance with semi-angle (*a*) $\alpha = 0.25$, (*b*) 0.50, (*c*) 0.75, (*d*)=1.0. Panel (*e*) shows a set of three-dimensional streamlines above a spherical protuberance that touches the plane wall corresponding to $\alpha = 1.0$, most of them emanating from the elevation $x/a = 0.10$.

in separated variables is available [12, 13]. When $(1 - \alpha)\pi < 2.548$ or $\alpha > 0.189$, the analytical solution reveals the formation of an infinite sequence of corner eddies whose size and strength is an exponentially decreasing function of radial distance from the apex. This analogy suggests that, close to the corner, the shear stress Σ_z shown in Figure 2(*a*) changes sign an infinite number of times on either side, but these small-scale fluctuations are not captured with adequate resolution by the numerical method.

In Figure 2(*b*), we present results for the shear stress corresponding to a hemispherical cavity with $\alpha = 0.50$. Comparing the shear-stress distributions with those depicted in Figure 2(*a*) reveals that the shape of Σ_y undergoes only minor changes, whereas that of Σ_z is changed in a significant manner. At the top of the protuberance, Σ_z attains a maximum value that is equal to four times the unperturbed value, but then it decreases rapidly and changes sign close
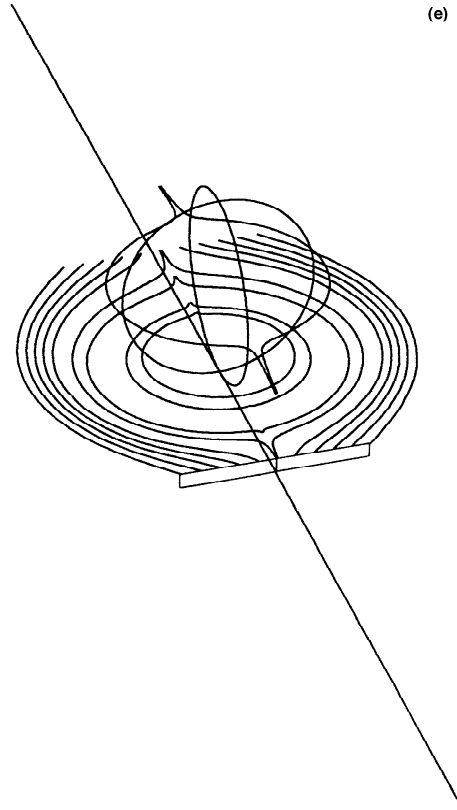
Figure 3. continued.

to the base, indicating the occurrence of a stagnation point. The angular position where Σ_z changes sign is found to be $\theta = 73.2°$, which is in excellent agreement with the analytical predictions of Price [5]. There is a similar change in sign of Σ_z along the plane wall, indicating the presence of a stagnation point at the radial position $\sigma = 1.22\,a$, which is also in perfect agreement with Price's predictions. It is tempting to interpret this behavior as evidence of flow reversal and onset of a region of recirculating flow in the xy plane with a dividing streamline beginning and ending at the two aforementioned stagnation points, but inspection of the streamline pattern, to be discussed below, will reveal a different kind of behavior.

The graphs of the shear-stress distributions for shapes with $\alpha = 0.75$ and 1.0, shown in Figures 2(*c, d*), reveal that Σ_z reaches, respectively, maximum values of nearly 5.5 and 6. The reversal of the sign at a sequence of points along the protuberance contour indicates the presence of multiple wall stagnation points, not all of which are the beginning or the end of dividing streamlines enclosing regions of recirculating flow. Close to the base corner, the distribution of Σ_y obtains a concave shape, reflecting the shape of the narrow gap forming between the surface of the protuberance and the wall in the xz plane. This behavior is consistent with an approximate local analysis conducted under the assumptions of locally unidirectional lubrication flow.

3.3. STREAMLINE PATTERNS

To illustrate the structure of the flow in an explicit manner, in Figures 3(*a–d*) we present the streamline patterns in the xy plane for the four shapes corresponding to Figures 2(*a–*
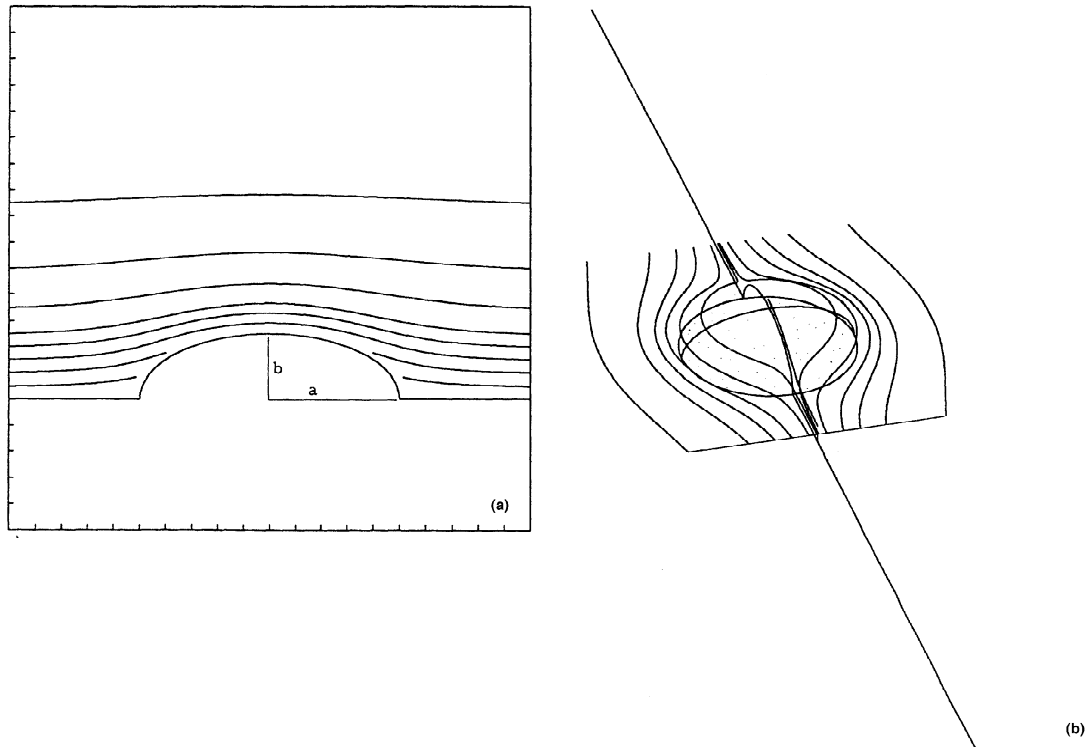
Figure 4. (*a*) Streamline patterns in the xy plane of flow over a semi-spheroidal protuberance with aspect ratio $b/a = 0.50$ and $\alpha = 0.50$. (*b*) A set of three-dimensional streamlines.

d). For the short protuberance with $\alpha = 0.25$, we observe that the streamlines follow the topography of the boundary, whereas for the taller protuberances we observe the occurrence of stagnation points at the boundaries. Concentrating in particular on Figure 3(*b*), we observe that the outermost stagnation points over the protuberance and the wall indicated by the short straight segments, identified by Price [5] and confirmed by the present results, do *not* connect a dividing streamline, but are nodal points of separation or attachment [2]. It might appear that this behavior violates conservation of mass, but one must keep in mind that the rate of expansion of the pseudo two-dimensional flow in the xy plane is finite owing to the extension of the fluid parcels in the azimuthal direction. The innermost stagnation points are expected to connect dividing streamlines that enclose regions of recirculating flow as predicted by the aforementioned local similarity solution. As α is increased, the protuberance tends to obtain the shape of a whole sphere, and the outermost stagnation point over its surface shifts towards the protuberance mid-plane. Correspondingly, the outermost stagnation point over the wall moves further away from the point of contact.

A more direct illustration of the three-dimensional structure of the flow is depicted Figure 3(*e*), where we plot a family of streamlines corresponding to flow past a whole sphere. The significant diversion of fluid-particle paths and the absence of regions of recirculating flow are two important features. All fluid parcels spend a finite amount of time near the protuberance, and none of them becomes trapped within eddies; the azimuthal motion provides a route for escape. Note that this would not be true for the analogous case of shear flow over a cylindrical protuberance in two-dimensional flow, where fluid particles trapped within eddies remain there for an infinite amount of time.

Table 2. The y component of the force, F_y, and the z component of the torque with respect to the origin, T_z, exerted on a protuberance whose shape is half an oblate spheroid with center at the wall, corresponding to $\alpha = 1/2$.

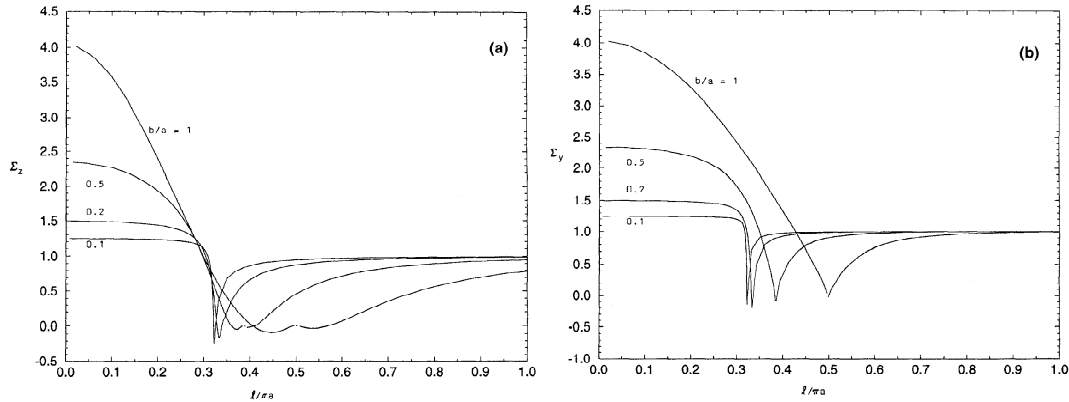| b/a	$F_y/\pi\mu k a^2$	$T_z/\pi\mu k a^3$
1.0	4.30	2.45
0.5	2.43	0.613
0.2	1.51	0.111
0.1	1.24	0.030

Figure 5. Shear flow over a hemispheroidal protuberance adhering to a plane wall for different aspect ratios b/a. (*a*) Dimensionless shear stress along the trace of the protuberance and of the wall in the xy plane, $\Sigma_z = \sigma_z/k\mu$; (*b*) Dimensionless shear stress along the corresponding boundary trace in the xz plane, $\Sigma_y = \sigma_y/k\mu$. Both are plotted with respect to reduced arc length, $l/\pi a$, measured along the respective traces of the boundary with origin at the axis of symmetry.

3.4. SPHEROIDAL SHAPES

In the second part of the numerical studies, we consider flow past oblate spheroidal protuberances whose axis of revolution is perpendicular to the wall as illustrated in Figure 4(*a*). Our main objective is to demonstrate the significance of the protuberance aspect ratio b/a, where a is the major radial axis and b is the minor x semi-axis; $b/a=1$ yields a spherical protuberance considered before.

In Table 2, we present the y component of the force, F_y, and the z component of the torque with respect to the origin, T_z, acting on a protuberance whose shape is half an oblate spheroid with center at the wall, corresponding to $\alpha = 1/2$; $b/a = 1$ yields a hemisphere. Not surprisingly, we find that both the force and the torque decrease by a significant factor as b/a and thus the height of the protuberance becomes smaller. In this limit, because the surface of the protuberance becomes flat, the torque tends to vanish, whereas the force tends to become equal to that exerted on its base due to the unperturbed shear flow; the corresponding entry in Table 2 tends to unity. Even for the shortest protuberance, however, with $b/a = 0.10$, there is a 25% difference between the asymptotic and the actual value.

In Figure 5 (*a, b*), we present the distribution of the dimensionless shear stresses Σ_z and Σ_y, both plotted with respect to reduced arc length, $l/\pi a$, measured along the respective traces

of the wall with origin at the top of the protuberance. As the aspect ratio b/a is decreased, both distributions tend to flatten over the main portion of the protuberance and exhibit sharp variations near the rim; the corresponding distributions over the wall show similar behaviors. It is important to note that, even for the shortest protuberance with $b/a = 0.1$, the shear stress at the top is higher than that of the undisturbed flow by a factor that is approximately equal to 1.25, which indicates once more that neglecting the perturbation flow may lead to significant quantitative error and erroneous interpretations. For all aspect ratios, the aforementioned local similarity solution can be used to describe the flow near the rim, revealing the presence of an infinite series of regions of recirculating flow in the xy plane with associated oscillations in shear stress.

In Figures 4(*a, b*), we present the streamline patterns in the xy plane, and fluid particle paths off the plane of symmetry for flow over a protuberance with aspect ratio $b/a = 0.50$. The streamlines follow the topography of the boundary in the xy plane, but there are inconspicuous eddies near the rim. The general kinematical fractures of the flow are similar to those described before for the spherical shapes.

In summary, we have developed and implemented a boundary integral method for representing and computing simple shear flow over a plane wall with axisymmetric protuberances, and applied it to obtain numerical results for two families of protuberance shapes. The demonstrated efficiency of the method makes it attractive in studies of pure hydrodynamics or convective scalar transport. Furthermore, the method can be extended in a straightforward manner to handle an incident parabolic flow associated with an imposed pressure gradient.

Acknowledgments

References

1. J.J.L. Higdon, Stokes flow in arbitrary two-dimensional domains: shear flow over ridges and cavities. *J. Fluid Mech.* 159 (1985) 195–226.
2. M. Tobak and D.J. Peake, Topology of three-dimensional separated flows. *Annu. Rev. Fluid Mech.* 14 (1982) 61–85.
3. M.E. O'Neill, A sphere in contact with a plane wall in a slow linear shear flow. *Chem. Eng. Sc.* 23 (1968) 1293–1298.
4. W.A. Hyman, Shear flow over a protrusion from a plane wall. *J. Biomechanics* 5 (1972) 45–48, Corrigendum on page 643.
5. T.C. Price, Slow linear shear flow past a hemispherical bump in a plane wall. *Q.J. Mech. Appl. Math.* 38 (1985) 93–104.
6. C. Pozrikidis, *Boundary integral and singularity methods for linearized viscous flow*. Cambridge: Cambridge University Press (1992) 259pp.
7. C. Pozrikidis, Shear flow over a plane wall with an axisymmetric cavity or a circular orifice of finite thickness. *Phys. Fluids* 6 (1994) 68–79.
8. C. Pozrikidis, The motion of particles in the Hele-Shaw cell. *J. Fluid Mech.* 261 (1994) 199–222.
9. S. Kim and S. Karrila, *Microdynamics: Principles and selected applications.* (1991) 507pp.
10. M. Abramowitz and I.S. Stegun, *Handbook of mathematical functions*. Dover (1972) 1045pp.
11. A.M.J. Davis and M.E. O'Neill, Separation in a slow linear shear flow past a cylinder and a plane. *J. Fluid Mech.* 81 (1977) 551–564.
12. C. Pozrikidis, *Introduction to theoretical and computational fluid dynamics*. Oxford: Oxford University Press (1996) 673pp.
13. H.K. Moffatt, Viscous and resistive eddies near a sharp corner. *J. Fluid Mech.* 18 (1964) 1–18.